Theoretical and Computational Acoustics
D. Lee, Y-H Pao, M.H. Schultz, and Y-C Teng (Editors)


# Influence of Signal Band-Limitation on the Resolution of Travel-Time Tomography: 2-D Numerical Experiments

Enrico Priolo
Osservatorio Geofisico Sperimentale
P.O. Box 2011, 34016 Trieste, Italy

Claudio Chiaruttini
DINMA, Università di Trieste
v. A. Valerio 10, 34127 Trieste, Italy

Alessandro Pregarz
Osservatorio Geofisico Sperimentale
P.O. Box 2011, 34016 Trieste, Italy

**Abstract**

Resolution analysis of travel-time tomographic inversion of seismic records is essential for correct data interpretation. If infinite signal bandwidth can be assumed, then asymptotic ray theory provides the convenient framework to state the problem and to model delays. In seismic experiments, however, infinite bandwidth is a highly idealized situation, and the effect of band-limitation needs to be carefully considered. Wave theory shows that bandlimited signals propagate from source to receiver along "physical" rays, or Fresnel rays, with finite cross-section instead of the infinitely thin "mathematical" rays. For a given medium velocity, the cross-section radius depends on bandwidth and source-receiver distance. Rytov approximation of the scattering problem can be used to analyze the sensitivity of recorded time delays to small velocity perturbations in wave transmission experiments. This theory leads to the counter-intuitive prediction that the greatest delay is obtained by perturbations off the mathematical ray, though still within the Fresnel ray. The paradox gets striking in 3-D geometry: a point perturbation on the mathematical ray produces no delay, and is therefore undetectable. We use 2-D modeling of the full wave equation to investigate numerically this paradox, and more generally, the resolution of bandlimited seismic records.

## 1. Introduction

Tomographic imaging in Geophysics is mostly based on ray-theoretic travel-time tomography [3]. Asymptotic ray theory assumes that signals have infinite bandwidth; in practice, this requirement means that velocity anomalies should be smooth enough to be correctly recovered. This condition hardly holds in geophysical exploration: the earth's crust has significant heterogeneities of smaller extension than the wavelengths used to sample them. Consequently, the resolution given by ray-theoretic tomography is illusive and not all details appearing in the images are reliable. It is known that the effective resolution of a tomographic experiment is given by the Fresnel radius, which is

a square root function of both the signal dominating wavelength and the source-receiver distance.

When ray theory assumptions do not hold, the problem may be correctly handled by diffraction tomography, which fully accounts for wave phenomena [12,4]. However, this method is stated in the frequency domain and requires continuous sources and long observation times; such experimental conditions are at odds with seimic acquisition requirements. To overcome these difficulties, Woodward and Rocca[15,16] proposed the wave-equation tomography, which is stated in the time domain and accounts for diffraction effects. This theory allows to discuss the effective resolution of travel-time tomography with band-limited signals. Based on the Rytov solution to the weak scattering problem, it leads to the counter-intuitive prediction that the greatest delay is obtained with velocity perturbations off the mathematical ray (the Fermat's path), though still within the Fresnel radius. The paradox gets striking in a 3-D geometry: a point perturbation on the mathematical ray produces no delay, and is therefore undetectable. We use 2-D spectral element modeling of the full wave equation to investigate numerically this paradox and, more generally, resolution of band limited seismic records. The setting of the numerical simulations reproduces a seismic experiment of cross-well tomography.

Section 2 introduces the analytical theory; Section 3 describes the numerical model and modeling technique; the results of the simulation are discussed in Section 4.

## 2. The theory

### 2.1. *Mathematical raypaths*

Travel-time tomography solves the problem of recovering an unknown velocity field from arrival-time measurements of acoustic or seismic waves. The integral equation representing the problem is

$$t(\mathbf{g};\mathbf{s}) = \int w(\mathbf{r})\, L[\mathbf{r};\mathbf{s},\mathbf{g},w(\mathbf{r})]\, d\mathbf{r}\,, \tag{2.1}$$

where $t$ is the travel-time between the source $\mathbf{s}$ and the receiver (geophone) $\mathbf{g}$, $\mathbf{r}$ is the position vector, $w = 1/c$ is the slowness (reciprocal of velocity) in the medium, $L$ is a distribution representing the raypath [i.e., $+\infty$ along the ray, 0 elsewhere]. This equation is nonlinear in $w$, since it appears both as a factor in the integrand and as an argument of $L$. If we decompose the unknown slowness field in a known background field $w_0$ plus a small perturbation $\Delta w$, equation (2.1) can be linearized as:

$$\Delta t(\mathbf{g};\mathbf{s}) = \int \Delta w(\mathbf{r})\, L_0[\mathbf{r};\mathbf{s},\mathbf{g},w_0(\mathbf{r})]\, d\mathbf{r}, \tag{2.2}$$

where $\Delta t$ is the time delay of the measured signal with respect to the travel-time $t_0$ in the background medium [1]. This expression is a generalized Radon transform, meaning that the unknown perturbed velocity field is sampled with line integral projections over unperturbed raypaths $L_0$. The raypath represents the resolving kernel of ray tomography: having vanishing thickness, resolution is complete in any direction normal to the ray, while it is null along the ray. The aim of tomographic inversion algorithms is then the recovery of the unknown velocity field from data obtained with a dense coverage of rays.

In the simplest instance of tomography, rays are straight lines, as when the background medium is assumed homogeneous. For instance in a 2-D space, if we represent

straight lines in polar coordinates $(p, \phi)$, with $p$ the distance from the origin and $\phi$ the normal direction, the inverse Radon transform takes the well known form[3]:

$$\Delta w(\mathbf{r}) = \int_0^{\pi} \Delta t^*[p(\mathbf{r}, \phi), \phi]\, d\phi, \tag{2.3}$$

with

$$\Delta t^*(p, \phi) = -\frac{1}{2\pi^2} \Delta t(p, \phi) * \frac{1}{p^2}. \tag{2.4}$$

In (2.3) the function $p(\mathbf{r}, \phi)$ maps the angle $\phi$ in the radial parameter of the straight line with angle $\phi$ through $\mathbf{r}$. The equation makes thus clear that the solution for $\Delta w$ is obtained "backprojecting" filtered data $\Delta t^*$ over straight rays; the asterisk operator in (2.4) indicates convolution with respect to variable $p$. The inverse Radon transform can be generalized to the case of curved rays.

### 2.2. *Monochromatic wavepaths*

Ray theoretic tomography is rooted either in the eikonal equation or in the Fermat's principle, and is therefore valid in the asymptotic limit of high frequency—i.e.: when the slowness perturbation wavelengths are much larger than the signal wavelength. Otherwise, the full wave equation has to be considered. Under some limiting assumptions concerning an appropriate knowledge of the source wavelet and the availability of noise-free data, two wave-theoretic equivalents of equation (2.2) can be obtained by linearizing the scalar wave equation according to either Born and Rytov methods[15]. Born approximation is suitable to describe the backscattered field, as in reflection problems. In the case of transmission experiments (i.e.: forward scattering), the Rytov approximation is more appropriate [6].

#### 2.2.1. *Rytov approximation*

The Rytov approximation is based on the representation of the wavefield by an exponential with complex argument $\Psi = \exp(\Phi)$. In such a way, the real part of $\Phi$ accounts for the wave amplitude, and the imaginary part for the phase. This decomposition in amplitude and phase is a further reason to use this approximation in tomography, since phase can be directly related to travel time. The Rytov weak scattering approximation relates linearly the wavefield rate of change $\Delta\Phi$ with the *objective function* $O$ — representing the velocity anomaly — and the incident wavefield $\Psi_0$. It is written as:

$$\Delta\Phi(\mathbf{g}; \mathbf{s}) = \int O(\mathbf{r}) \frac{G_0[\mathbf{g}; \mathbf{r}, c_0(\mathbf{r})]\Psi_0[\mathbf{r}; \mathbf{s}, c_0(\mathbf{r})]}{\Psi_0[\mathbf{g}; \mathbf{s}, c_0(\mathbf{r})]}\, d\mathbf{r}, \tag{2.5}$$

$$O(\mathbf{r}) = k_0^2(\mathbf{r}) \left[1 - \frac{c_0^2(\mathbf{r})}{c^2(\mathbf{r})}\right] \approx 2k_0^2(\mathbf{r}) \frac{\Delta c(\mathbf{r})}{c(\mathbf{r})}, \tag{2.6}$$

where $k_0$ is the background wavenumber, and $G_0$ is the Green's function of the background medium, given in 3-D by

$$G_0(\mathbf{r}) = \frac{\exp(ik_0|\mathbf{r}|)}{4\pi|\mathbf{r}|}, \tag{2.7}$$

and in 2-D by

$$G_0(\mathbf{r}) = \frac{i}{4} H_0^{(1)}(k_0|\mathbf{r}|). \tag{2.8}$$

$H_0^{(1)}$ is the zero-order Hankel function of the first kind.

For a point source, the unperturbed wavefield $\Psi_0$ reduces to the Green's function $G_0$. With this substitution, and making the dependence on the velocity explicit, by using the approximate expression (2.6) for the object function $O$, the Rytov formula (2.5) is written as:

$$\Delta\Phi(\mathbf{g};\mathbf{s}) = \int \frac{\Delta c(\mathbf{r})}{c(\mathbf{r})} \mathcal{L}_0(\mathbf{r};\mathbf{s},\mathbf{g})\, d\mathbf{r}. \tag{2.9}$$

Woodward [15] calls the symbol

$$\mathcal{L}_0(\mathbf{r};\mathbf{s},\mathbf{g}) = 2k_0^2(\mathbf{r}) \frac{G_0[\mathbf{r};\mathbf{g},c_0(\mathbf{r})] G_0[\mathbf{r};\mathbf{s},c_0(\mathbf{r})]}{G_0[\mathbf{g};\mathbf{s},c_0(\mathbf{r})]} \tag{2.10}$$

the Rytov "wavepath", for the formal analogy between equations (2.9) and (2.2).

$\mathcal{L}_0$ is the resolving kernel in wave-theoretic tomography. It is an oscillating function with amplitude decaying as $|\mathbf{r}|^{-1}$ for the 2-D case and as $|\mathbf{r}|^{-2}$ for the 3-D case, in the limit $|\mathbf{r}| \to \infty$; in the same limit, the radial wavelength approaches half the wavelength. The zeros of the imaginary part of the Rytov wavepaths are confocal ellipses and ellipsoids in the 2-D and 3-D spaces, respectively. They are the boundaries of the Fresnel volumes, i.e.: regions from where diffracted energy interferes either constructively or destructively with the direct arrival. The innermost Fresnel volume is the Fresnel ray.

The necessary condition for Rytov approximation to be valid [12] is that the phase change over a single wavelength be small, that is:

$$\frac{\Delta c}{c} \gg \left( \frac{\lambda}{2\pi} \nabla\Phi \right)^2 . \tag{2.11}$$

Note that the size of the object is not a limiting factor in the Rytov approximation; it is only required that the wavefiled change over a wavelength be small.

### 2.3. *Bandlimited raypaths*

A long observation time is necessary for the precise determination of phase shifts, the wave theoretic equivalents of ray theoretic time delays. The main drawback of this requirement, in seismic experiments, is that long observation times result in contamination of the recorded time series with noise and later arrivals. To reconcile wave-equation tomography with time-delay tomography, Woodward [15] maps the immaginary part of phase perturbation $\Im[\Delta\Phi]$ to time dividing it by $\omega$. In the hypothesis that phase is linear with frequency (no dispersion), the time thus obtained is frequency independent. The no dispersion condition is an approximation not only in the real world, but even in simpler models. For instance, in an homogeneous medium where the velocity field varies rapidly on the scale of the source wavelength, wavelets are affected by geometrical frequency dispersion [15]. This condition can be partly relaxed taking the average of wave-theoretic time-delays over the bandwidth:

$$\Delta t = \frac{1}{\Delta\omega} \int_{\omega_1}^{\omega_2} \frac{\Im[\Delta\Phi(\omega)]}{\omega}\, d\omega. \tag{2.12}$$

Using equation (2.9), it is convenient to write the above expression as

$$\Delta t = \int \frac{\Delta c(\mathbf{r})}{c(\mathbf{r})} L_{\Delta\omega}(\mathbf{r}) d\mathbf{r}\ , \tag{2.13}$$

where

$$L_{\Delta\omega}(\mathbf{r}) = \frac{1}{\Delta\omega}\int_{\omega_1}^{\omega_2} \frac{\Im[\mathcal{L}_0(\omega,\mathbf{r})]}{\omega}\, d\omega \tag{2.14}$$

is the bandlimited raypath, which is the resolving kernel for bandlimited time-delay tomography.

In equation (2.14), all signal components are assumed to have equal energy, or, in other words, the signal Fourier spectrum is a box-car function. For a signal characterized by a generic bandlimited spectrum $\mathcal{F}(\omega)$, we use for equation (2.14) the more general form

$$L_{\mathcal{P}(\omega)}(\mathbf{r}) = \int_0^\infty \mathcal{P}(\omega)\frac{\Im[\mathcal{L}_0(\omega,\mathbf{r})]}{\omega}\, d\omega, \tag{2.15}$$

where $\mathcal{P}(\omega) = |\mathcal{F}(\omega)|^2 \,/\, \int_0^\infty |\mathcal{F}(\omega)|^2 d\omega$ is the normalized power spectrum of the unperturbed signal. Equations (2.14) and (2.15) can be seen as the resolution pattern corresponding to the given bandlimited signal.

For a point source in a 3-D space, the formal integration of (2.14) leads to:

$$L_{\Delta\omega}(\mathbf{r}) = \frac{1}{2\pi\Delta\omega[c\tau(\mathbf{r})]^2}\frac{|\mathbf{g}-\mathbf{s}|}{|\mathbf{r}-\mathbf{g}||\mathbf{r}-\mathbf{s}|}\left[\sin\left(\omega\,\tau(\mathbf{r})\right) - \omega\,\tau(\mathbf{r})\,\cos\left(\omega\,\tau(\mathbf{r})\right)\right]_{\omega_1}^{\omega_2}, \tag{2.16}$$

where

$$\tau(\mathbf{r};\mathbf{s},\mathbf{g}) = \frac{|\mathbf{r}-\mathbf{s}| + |\mathbf{r}-\mathbf{g}| - |\mathbf{g}-\mathbf{s}|}{c} \tag{2.17}$$

is the diffraction delay. It can be easily seen that $\tau(\mathbf{r};\mathbf{s},\mathbf{g}) = 0$ is the equation of the mathematical ray. For a point source in a 2-D space (3-D line source), the resolving kernel is:

$$\begin{aligned} L_{\Delta\omega}(\mathbf{r}) \;=\; & \frac{-1}{2\Delta\omega\sqrt{2}[c\tau(\mathbf{r})]^{\frac{3}{2}}}\sqrt{\frac{|\mathbf{g}-\mathbf{s}|}{|\mathbf{r}-\mathbf{g}||\mathbf{r}-\mathbf{s}|}} \\ & \left[2\sqrt{\frac{\omega\tau(\mathbf{r})}{\pi}}\,\cos\left(\omega\tau(\mathbf{r})+\frac{\pi}{4}\right) - C\left(\sqrt{\frac{2\,\omega\tau(\mathbf{r})}{\pi}}\right) + S\left(\sqrt{\frac{2\,\omega\tau(\mathbf{r})}{\pi}}\right)\right]_{\omega_1}^{\omega_2}, \end{aligned} \tag{2.18}$$

where $C$ and $S$ are the Fresnel integrals. The asymptotic approximation of the Hankel function

$$H_0^{(1)}(x) \approx \sqrt{\frac{2}{\pi x}}\exp[i(x-\pi/4)], \tag{2.19}$$

valid for large values of the argument ($x \gg 1$), was used to derive equation (2.19).

For a generic signal spectrum, equation (2.15) has no formal solution, and is to be integrated numerically.

Band-limited, or physical, rays are the volumes through which energy propagates from source to receiver, and may be considered, in some sense, as filtered mathematical rays in the pass-band $[\omega_1, \omega_2]$. They share common properties in both 3-D and 2-D spaces. They are symmetrical with respect to source and receiver and extend behind these points (Figure 1). Moreover, they have a singularity at source and receiver position, a fact which has some strong applicative implications. For instance, in seismic exploration on land, deep anomalies can be hidden by surface inhomogeneities close

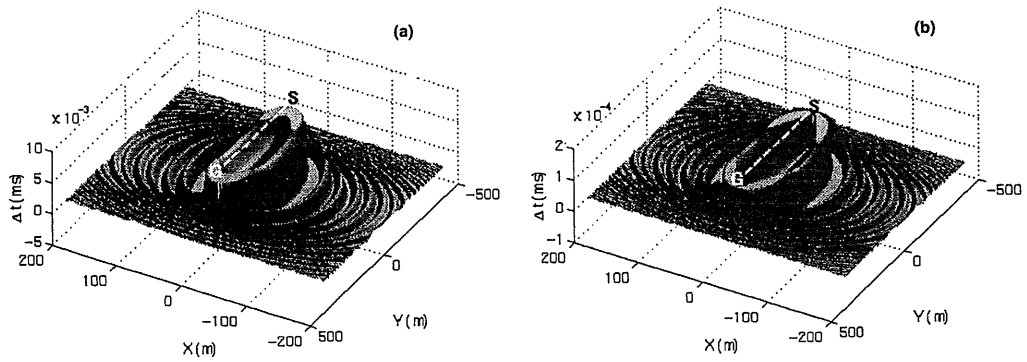


Fig. 1. Rytov bandlimited raypaths. (a) 2-D, and (b) 3-D. In the 3-D case, a longitudinal slice across the raypath is represented. The source-receiver distance is 519.2m and the signal has a constant energy distribution within a bandwith of [0Hz, 200Hz] (box-car energy power spectrum). A different scale is used for the two spatial directions.

to the source; careful analysis of the geophone sites is also necessary to obtain the so called "static corrections". A remarkable, and paradoxical, property is that they have a minimum across the mathematical ray. This is a property that Fresnel rays inherit from monochromatic wavepaths. From (2.16), the expression of 3-D wavepaths in the vicinity of the mathematical ray is controlled by the imaginary part of the exponential, that is a factor $\sin(\omega\tau(\mathbf{r}))$, vanishing for $\tau(\mathbf{r}) = 0$. The corresponding factor in 2-D space is $\sin(\omega\tau(\mathbf{r}) + \pi/4)$, which can be obtained from (2.19) using the approximation (2.19). The $\pi/4$ phase shift is responsible for the local minimum across the mathematical ray. Therefore, the counter-intuitive property holds that the greatest effect on travel-time is *not* obtained by a point perturbation of the medium located along the shortest-time path; moreover, in 3-D such a perturbation does not produce any effect at all. This does not mean, however, that the *wave* carries no information at all on the mathematical ray; it simply states this holds for the time (or phase) of signals. The information missing in time is carried by the wave amplitude, the resolution function of which is nearly in quadrature with the corresponding one in time. In this work, however, the investigation is restricted only to the phase of the signal.

For bandlimited signals, the width of the raypath depends inversely on the width of the frequency band and not on the central frequency[15]. The wider the band, the closer the ray theory is approximated. Echoing the uncertainty relation $\Delta t\ \Delta\omega = 2\pi$, the width of the bandlimited raypath, or bandlimited ray-width, can be computed from the width of the main lobe of its envelope[15] by

$$R_{\Delta\omega} = \sqrt{\frac{\pi c}{\Delta\omega}\left(\frac{\pi c}{\Delta\omega} + \mathsf{L}\right)}, \tag{2.20}$$

where $\mathsf{L}$ is the source-receiver distance, instead of the well known formula expressing the Fresnel radius for a monochromatic field $R_F = \frac{1}{2}\sqrt{(2\pi\, c\,/\,\omega)\ \mathsf{L}}$. The actual source frequency content changes significantly the resolution patterns. In both 2-D and 3-D spaces, accounting for a smoother spectrum, for instance the spectrum of a Ricker wavelet, puts more emphasis on the central part of the spectrum rather than on the extreme frequencies. This results in widening the main lobe, and damping ex-

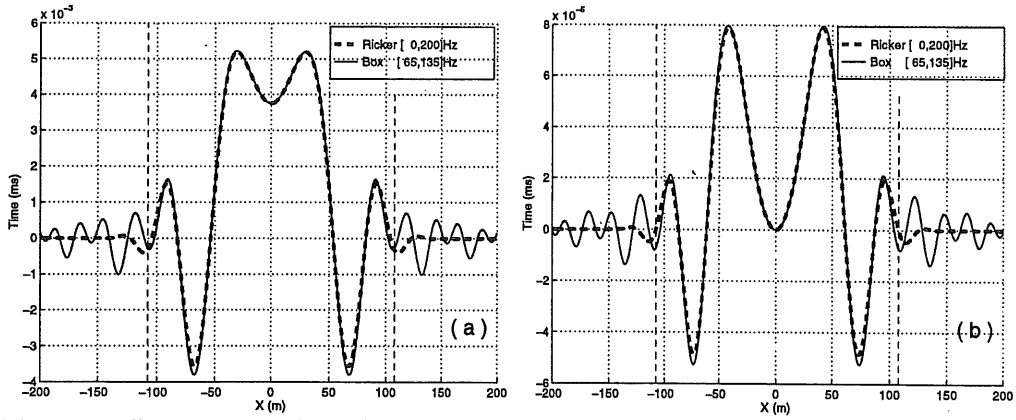


Fig. 2. Cross-section through the origin of Rytov bandlimited raypaths, for a Ricker wavelet spectrum and an "equivalent" spectrum with constant energy distribution. (a) 2-D, and (b) 3-D. Geometry as in Figure 1. Vertical dashed lines indicate the bandlimited raywidth, as computed by eq. (2.24).

ternal oscillations of the bandlimited raypath, which remains well bounded within the bandlimited ray-width.

Figures 1 to 2 illustrates the previous discussion. Figure 1 shows an example of 2-D and 3-D bandlimited raypaths, for a signal characterized by a box-car spectrum with a bandwidth of [0Hz, 200Hz]. Figure 2 shows their maximal transversal sections (at the middle point between source and receiver) for a Ricker wavelet with a smooth energy spectrum within [0Hz, 200Hz], and an "equivalent" wavelet with constant energy distribution over a bandwidth of [65Hz, 135Hz]. For the raypaths of the Ricker wavelet, it can be clearly appreciated: (i) the reduction of the external oscillations due to the smooth frequency cut-off, (ii) and the modulating effect of the lowest frequency. The good agreement of the curves within the bandlimited ray-width shows also that a sharp frequency cut-off has effect mainly outside the bandlimited ray-width as a rippled pattern, thus reflecting the well known Gibb's phenomenon in time series analysis.

In the next session we simulate numerically a wave transmission experiment, to have a confirmation of the analytical prediction and to evaluate how much resolution is lost in both the 2-D and 3-D tomographic inversions of a 3-D experiment.

## 3. Numerical modeling

The Chebyshev spectral element method (SPEM) is a high-order finite element technique, which solves the variational formulation of the differential equation. The computational domain is decomposed into non-overlapping quadrilateral elements, and then, on each element, the solution of the variational problem is expressed as a truncated expansion of Chebyshev orthogonal polynomials, as in the spectral methods [8]. An investigation of SPEM and its application to the solution of both acoustic and elastic wave equations has been described elsewhere [7,9,10]. Polynomial orders six or eight are usually chosen. Time integration is performed by an implicit Newmark scheme, also called the Constant Average Acceleration, which is a two-step algorithm, unconditionally stable and second-order accurate.

In the present work, the numerical simulations consist of a family of 2-D acoustic models (Figure 3a) where a small velocity perturbation is located at half the source-

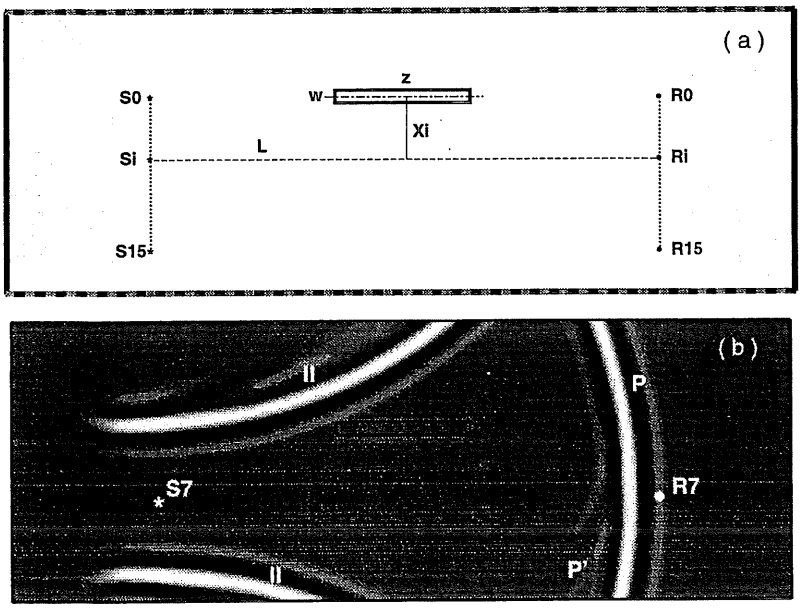


Fig. 3. SPEM model. (a) Model description. (b) Pressure field at time $t = 0.184$s for the simulation pertinent to the source-receiver couple (S7, R7). Letters indicate the main wavefront (P), the scattered wave (P'), and the two second-order reflections from model edges (II).

receiver distance. In our experiments, we keep the perturbation fixed, and move the source-receiver pair. The source-receiver distance is L = 519.2m, and the velocity of the background medium is $V = 3000$m/s. The source time history is a zero-phase Ricker wavelet with a central frequency $F_c = 100$Hz, and maximum frequency $2F_c$, resulting in a dominating wavelength $\lambda = 30$m. The bandlimited ray-width of $R_{\Delta\omega} \approx 107$m was computed from equation (2.20) for an equivalent bandwidth of [35Hz, 65Hz]. The numerical experiment consists of sixteen models, one for each offset. The perturbation offset X with respect to the source-receiver axis ranges from 0 to 1.13 times the bandlimited ray-width. The first two offsets are X0 = 0m, and X1 = w/2 = 6.5m. The others are equally spaced with increment $\Delta$X = 8.21m, up to X15 = 121.4m. The perturbation is a rectangle of size z × w = 138.4 × 13m$^2$, and velocity $V' = 3100$m. These values satisfy the weak scattering hypothesis.

The computational domain is decomposed into 17×46 Chebyshev quadrangles of order $N = 6$, for a total of 28531 nodes. The size of the typical element is 16.24m×16.24m, corresponding to $G \approx 5.5$ nodes per minimum wavelength. Radiating boundary conditions are used at the four external edges of the computational domain, to avoid internal reflections. At the two lateral boundaries (thick solid lines in Figure 3a), a six element wide absorbing strip (shaded area) is defined, where the amplitude of the pressure wavefield is gradually attenuated[2]. At the other two boundaries (thick dashed lines), the non-reflecting Smith's condition [13] is applied, according to which the wavefiled for an unbounded medium can be exactly computed as the average of the two solutions corresponding to Dirichlet (rigid boundary) and Neumann (free boundary) problems. However, this technique cannot remove high-order reflections, that can be avoided only by enlarging the computational model. In our case, we did find such spurious incoming

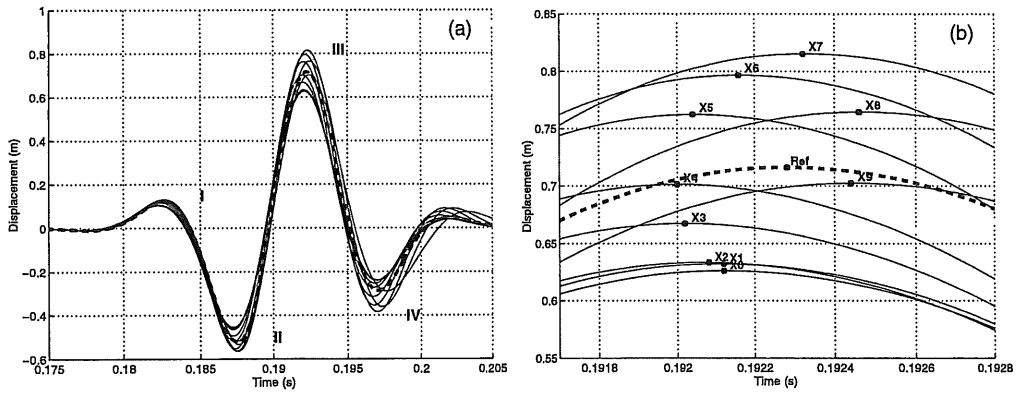


Fig. 4. SPEM synthetics. (a) Response at first ten offsets (X0 to X9) for the perturbed models (thin solid lines), and for the reference unperturbed model (thick dashed line). (b) Pulse (III). Cross marks and labels identify the points where the arrival time are estimated for each offset.

waves (II in Figure 3b), but only at late simulation times and always well distinct from the primary wavefield at the receivers. The computational time step is $\Delta t = 0.05$ms; it is much smaller than that required by the time integration scheme, but was chosen to allow detection of arrival time changes due to the velocity perturbation. The total time of simulation $T = 0.22$s allows the most energetic part of the wave to reach the receiver. Figure 3b shows a snapshot of the pressure field at time $t = 0.184s$. The effectiveness of the radiating boundaries conditions can be appreciated; in particular, the second-order reflections are far enough from the primary wavefield at receiver position.

## 4. Numerical results and discussion

Figure 4a shows all the synthetic time histories at first ten offsets $\{\mathrm{Xi}\}_{i=0,10}$, plus the reference homogeneous model. Arrival times are estimated in two different ways: i) in the time domain, by direct picking, and ii) in the frequency domain, with the Fourier phase spectrum.

In the frequency domain approach, a frequency dependent time delay between two seismograms, $\Delta t(\omega)$, can be directly computed for each offset from their phase shift $\Delta\phi(\omega)$, by the following equation:

$$\Delta t(\omega) = \frac{\Delta\phi(\omega)}{\omega}, \tag{4.21}$$

where each phase is computed from the Fourier phase spectrum of the whole signal. An example of the results obtained in our numerical experiments is given in Figure 5. Time delays appear to be stable in a neighbourhood of the central frequency (100Hz) and are highly variable in the high and low ends of the bandwidth. To determine an overall time delay, we assume that each $\Delta t(\omega)$ contributes to $\widetilde{\Delta t}$ with a weight proportional to the energy carried by the corresponding frequency, then resulting in the following equation:

$$\widetilde{\Delta t} = \int_0^\infty \mathcal{P}(\omega)\,\Delta t(\omega)\,d\omega, \tag{4.22}$$

where $\mathcal{P}(\omega)$ is the normalized power spectrum of the source. The effect of weighting $\Delta t(\omega)$ by $\mathcal{P}(\omega)$, and the resulting $\widetilde{\Delta t}$ is illustrated in the same figure. We can also

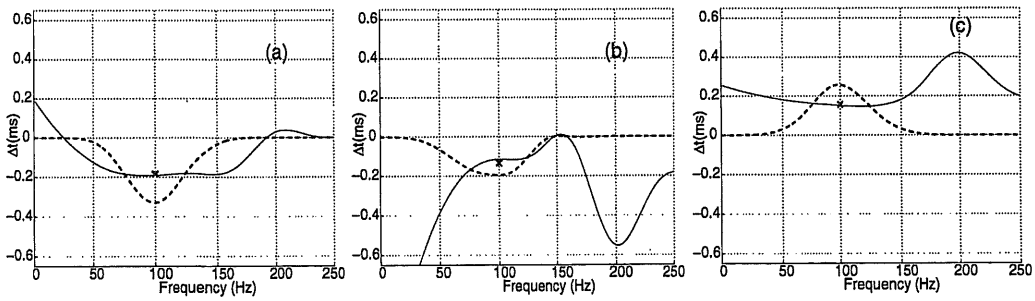


Fig. 5. Frequency dependent time delay $\Delta t(\omega)$ (solid line) estimated from signal phase at offsets X0 = 0m (a), X7 = 55.2m (c), and X10 = 71.5m (d). The result of weighting $\Delta t(\omega)$ by the source power spectrum is shown by the dashed line; for graphical purposes, these values are amplified by a factor 100. The resulting frequency independent time delay $\widetilde{\Delta t}$ is marked by a cross placed at the central frequency (100Hz).

see that the same value $\widetilde{\Delta t}$ would have obtained by averaging values of $\Delta t(\omega)$ on a narrower band centered at the central frequency.

Equation (2.12) maps phase shifts into time delays, but gives no information on which feature of the time history the delay concerns. In this respect, more insight is obtained by estimating time arrivals from time histories. In the time domain, we picked the extreme of the first four pulses, labelled I - IV in Fig. 4a. Figure 4b shows the picking for the strongest pulse. The resulting four families of delays are displayed in Fig. 6. For all of them, the delay at zero or small offsets is not the largest, as it would be intuitively expected, but a local minimum. The third, more energetic pulse is the one whose behaviour and values exactly conforms to Rytov's theory: the greatest time corresponds to a substantial offset. Numerical results suggest that the closer to signal onset the arrival time is picked, the more the intuitive behaviour is satisfied, but the corresponding delay value difforms from theory. In the case of a minimum-phase wavelet, where energy is concentrated at signal onset, time delays estimated at the first pulse would have presumably conformed to Rytov's theory. Time picking method comes out as a crucial matter, needing a deeper investigation.

Figure 7 compares the theorerical time delays to the time delays obtained from SPEM synthetics. Comparing the numerical results we can argue that the time delay i) is closely linked to the most energetic part of the time history, and ii) can be identified with no ambiguity in the frequency domain by taking into account the spectral energy of the signal. The good agreement betweeen numerical and theoretical values can be

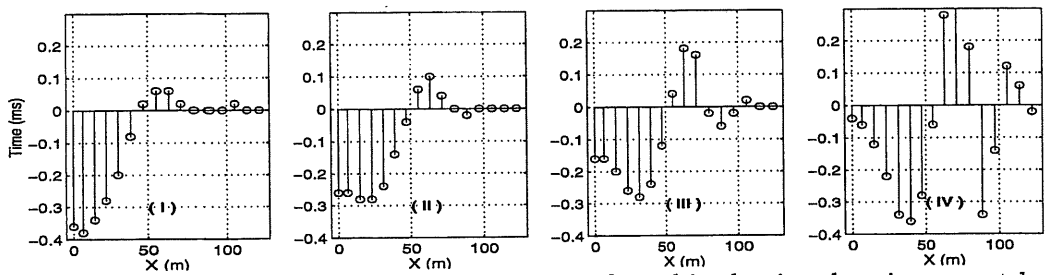


Fig. 6. Time delays versus offset. Estimation is performed in the time domain, separately for each pulse of the signal. Pulses are labeled according to Fig. 4a.

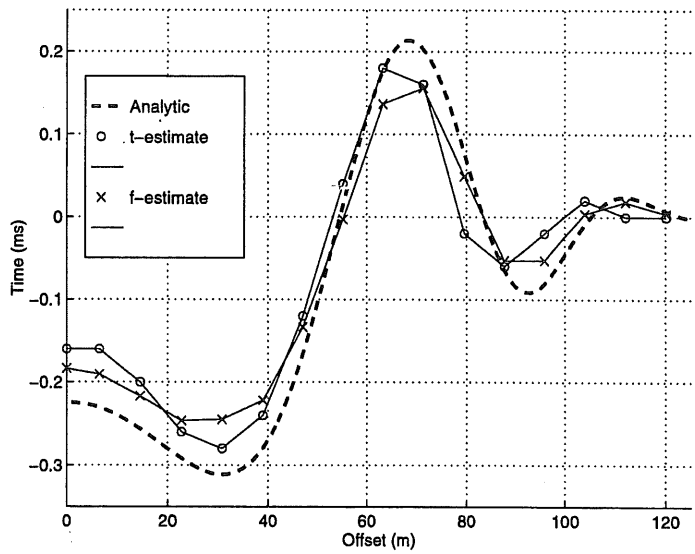


Fig. 7. Time delays versus offset for the 2-D model. The figure compares the theoretic curve (thick-dashed curve) with experimental values estimated in the time domain (circle marks and thin solid line), and in the frequency domain (cross marks and thin dashed line).

appreciated, in particular the lower magnitude of the delays at offset zero.

## 5. Conclusion

We used 2-D SPEM modeling of the acoustic full wave equation to reproduce the setting of a cross-well experiment with band-limited energy. We investigated in detail how the scattered wavefield depends on the offset from the mathematical ray of a small and localized velocity anomaly.

The dependence of time delays on offset conforms to the theoretical prediction if the arrival time is picked at the strongest peak of the time history. This confirms both the oscillatory character of the raypaths, and the paradox of the presence of a minimum delay across the mathematical raypath: a velocity anomaly close to it can be recovered only in part. The amount of information loss is greater in 3-D than in 2-D. Furthermore, information from single rays is ambiguous, since the time delay of a positive anomaly can be accounted for by a negative anomaly placed in the minima of the band-limited raypath. The effective resolution of a tomographic experiment with a bandlimited signal is given by the bandlimited ray-width, this concept replacing that of Fresnel radius valid for a monochromatic signal.

Our simulations with signals with a smooth energy spectrum shows that it is possible to define an equivalent bandwidth, with constant spectral energy level therein, which closely reproduces the band-limited raypath within the bandlimited Fresnel volume. Outside this volume, signals with a smooth spectral energy distribution rapidly vanish, whereas signals with sharp cut-offs show a slowly decaying ringing that closely reflects the well known Gibb's phenomenon.

## 6. Aknowledgments

This research was partly founded by the European Union (Contract JOU2-CT93-0321). Authors whish to thank Rinaldo Nicolich and Aldo Vesnaver for the useful discussions.

## 7. References

1. G. Beylkin. Imaging of discontinuities in the inverse scattering problem by inversion of causal generalized Radon transform. *J. Math. Phys.*, 26:99–108, 1985.
2. C. Cerjan, D. Kosloff, R. Kosloff, and M. Reshef. A nonreflecting boundary condition for discrete acoustic and elastic wave equations. *Geophysics*, 50:705–708, 1985.
3. C.H. Chapman. The Radon transform and seismic tomography. In G. Nolet, editor, *Seismic Tomography*, pages 25–47. Reidel, 1987.
4. A. J. Devaney. Geophysical diffraction tomography. *IEEE Trans. Geosci. Remote Sensing*, GE-22 fR(1):3–13, 1984.
5. G. Nolet. Seismic wave propagation and seismic tomography. In G. Nolet, editor, *Seismic Tomography*, pages 1–23. Reidel, 1987.
6. M. L. Oristaglio. Accuracy of the Born and Rytov approximations for reflection and refraction at a plane interface. *J. Opt. Soc. Am.*, 2(11):1987–1993, November 1985.
7. E. Padovani, E. Priolo, and G. Seriani. Low- and high-order finite element method: Experience in seismic modeling. *J. Comp. Acoustics*, 2(4):371–422, 1994.
8. A. T. Patera. A spectral element method for fluid dynamics: Laminar flow in a channel expansion. *J. Comp. Physics*, 54:468–488, 1984.
9. E. Priolo and G. Seriani. A numerical investigation of Chebyshev spectral element method for acoustic wave propagation. In R. Vichnevetsky, editor, *Proc. 13th IMACS Conf. on Comp. Appl. Math.*, volume 2, pages 551–556, Dublin, 1991. Criterion Press.
10. G. Seriani and E. Priolo. High-order spectral element method for acoustic wave modeling. In *Expanded Abstracts of SEG 61st Ann. Int. Mtg., Houston, Texas*, volume 2, pages 1561–1564. Soc. Expl. Geophys., 1991.
11. G. Seriani and E. Priolo. Spectral element method for acoustic wave simulation in heterogeneous media. *Finite Elements in Analysis and Design*, 16:337–348, 1994.
12. M. Slaney, A. C. Kak, and L. E. Larsen. Limitations of imaging with first-order diffraction tomography. *IEEE Trans. Microwave Th. Tech.*, MTT-32:860–873, 1984.
13. W. D. Smith. A nonreflecting plane boundary for wave propagation problems. *J. Comp. Physics*, 15:492–503, 1974.
14. P. R. Williamson and M. H. Worthington. Resolution limits in ray tomography due to wave behaviour: Numerical experiments. *Geophysics*, 58(5):727–735, may 1993.
15. M. J. Woodward. Wave-equation tomography. *Geophysics*, 57(1):15–26, 1992.
16. M. J. Woodward and F. Rocca. Wave-equation tomography. In *Expanded Abstracts of SEG 58th Ann. Int. Mtg., Anaheim (CA)*, volume 2, pages 1232–1235. Soc. Expl. Geophys., 1988.